



LAWRENCE
LIVERMORE
NATIONAL
LABORATORY

3D Hydrodynamics of the Deceleration Stage in ICF

C. R. Weber, D. S. Clark, A. W. Cook, D. C. Eder, S. W. Haan, B. A. Hammel, D. E. Hinkel, O. S. Jones, M. M. Marinak, J. L. Milovich, P. K. Patel, H. F. Robey, J. D. Salmonson, S. M. Sepke, C. A. Thomas

November 21, 2014

Physics of Plasmas

Disclaimer

This document was prepared as an account of work sponsored by an agency of the United States government. Neither the United States government nor Lawrence Livermore National Security, LLC, nor any of their employees makes any warranty, expressed or implied, or assumes any legal liability or responsibility for the accuracy, completeness, or usefulness of any information, apparatus, product, or process disclosed, or represents that its use would not infringe privately owned rights. Reference herein to any specific commercial product, process, or service by trade name, trademark, manufacturer, or otherwise does not necessarily constitute or imply its endorsement, recommendation, or favoring by the United States government or Lawrence Livermore National Security, LLC. The views and opinions of authors expressed herein do not necessarily state or reflect those of the United States government or Lawrence Livermore National Security, LLC, and shall not be used for advertising or product endorsement purposes.

3D Hydrodynamics of the Deceleration Stage in ICF

C. R. Weber,¹ D. S. Clark,¹ A. W. Cook,¹ D. C. Eder,¹ S. W. Haan,¹ B. A. Hammel,¹ D. E. Hinkel,¹ O. S. Jones,¹ M. M. Marinak,¹ J. L. Milovich,¹ P. K. Patel,¹ H. F. Robey,¹ J. D. Salmonson,¹ S. M. Sepke,¹ and C. A. Thomas¹

*Lawrence Livermore National Laboratory, Livermore, California 94550,
USA*

(Dated: 23 October 2014)

The deceleration stage of Inertial Confinement Fusion (ICF) implosions is modeled in detail using three-dimensional simulations designed to match experiments at the National Ignition Facility (NIF). In this final stage of the implosion, shocks rebound in the center of the capsule, form the high temperature, low density hot spot, and slow the incoming fuel. The flow field that results from this process is highly three-dimensional and influences many aspects of the implosion. The interior of the capsule has high-velocity motion, but viscous effects limit the range of scales that develop. The bulk motion of the hot spot shows relative agreement with experimental velocity measurements, while the second moment of the velocity would broaden the DT neutron spectrum, increasing the inferred temperature by 400 eV. Jets of ablator material are broken apart and redirected as they enter this dynamic hot spot. Two fundamentally different rad-hydro codes are used for this model and are in good agreement, adding confidence to this ICF model.

I. INTRODUCTION

High convergence Inertial Confinement Fusion (ICF) experiments at the National Ignition Facility (NIF)¹ have struggled with implosions that deviate far from their desired clean, 1D state². Implosion performance is degraded by asymmetric features such as a non-uniform radiation flux, perturbations on the capsule surfaces, and the presence of the capsule support tent and fill tube. Experimental evidence shows that these asymmetries result in swings in the in-flight shape of the capsule and in the final hot-spot shape³. Some implosions are polluted by ablator material mixing into the hot spot^{4,5}. When compared with 1D, no alpha-deposition simulations, these effects reduce the experimental yield by $\sim 10\times$, which is a factor of 4 worse than that anticipated⁶. Ultimately the goal in ICF design is to control the implosion to recover performance closer to 1D. Recent experiments have demonstrated that this is possible with modifications to the shape of the laser pulse⁷⁻⁹. These modifications reduce both hydrodynamic instability growth and overall compression. To achieve ignition, ICF designs are required that achieve higher levels of compression and will likely be accompanied by non-1D behavior. Therefore, it is important to understand the dynamics that occur in these non-ideal implosions, how they affect performance, and how they translate into diagnostic signatures.

Modeling NIF implosions have advanced to give a more-accurate picture of the final state of the implosion. Capsule-only simulations are now able to include the as-shot surface perturbations in 3D with resolution of up to 100 Legendre modes^{10,11}. Hohlräum modeling is producing a better understanding of the relationship between radiation asymmetries and the shape of the capsule^{12,13}. Finally, the effects of the capsule support tent and fill tube are now better-understood and included in post-shot models¹⁴. When applied with its highest level of detail to an implosion during the National Ignition Campaign (NIC), these models reproduce most experimental observables reasonably well¹¹.

Post-shot capsule-only models use a radiation drive tuned to match the shock velocity and merger times of VISAR experiments¹⁵, the shell trajectory of conA experiments¹⁶, and the bang time (time of peak neutron production) of layered DT experiments¹⁷. Radiation flux asymmetries are obtained from integrated (hohlräum and capsule) simulations¹⁸. Here we focus on a 3D model of NIC experiment N120321. This implosion recorded the highest down-scattered ratio (DSR, the ratio of scattered to unscattered neutrons) of the DT implosions

during the NIC. This 3D model uses the actual perturbations that were measured on the outside surface of the capsule and on the ice layer, the specified spectrum of roughness on internal layers, and surrogate perturbations that reproduces the expected effects of the fill tube and the support tent. Added to the initial inner gas of the capsule is 200 ng of ablator material. This pre-imposed mix is motivated by experimental signatures of this implosion and may come from higher modes not resolved on this Legendre mode ($l \leq 100$) model. This model uses the radiation-hydrodynamics code HYDRA¹⁹ and the development of this 3D model and its comparison to experimental data is discussed in Clark *et al.*¹¹.

In this paper, the deceleration stage of this implosion is studied in further detail. In Sec. II, an overview of the deceleration stage is given, illustrating its 3D dynamics. In Sec. III, the final shape of the fuel is quantified, showing the low mode structure that results from the radiation asymmetries. Section IV discusses the energetics of the implosion, showing how the conversion of kinetic energy into internal energy is degraded by 3D features. The significant velocities present in the hot spot are quantified in this section. In this model, a jet of ablator material enters the hot spot and is distorted by the complex hot spot motion. This interaction is described in Sec. V. The hydrodynamics of this HYDRA model are compared against simulations using the Miranda code[?] in Sec. VI. Miranda is a high-order rad-hydro code used to study mixing[?] and has been used previously in comparisons with HYDRA^{29?}. Final concluding remarks are given in Sec. VII.

II. OVERVIEW OF THE DECELERATION STAGE

In the final stage of the implosion, the inward going shock wave reflects from the center, reverberates in the interior, then stagnates the incoming shell and heats the central gas. This stage is shown from a 1D simulation of NIC implosion N120321 in Fig. 1, which focuses on the central 300 μm and last 1.5 ns of the implosion. Here we see the shock wave reach the center at 21.9 ns, bounce off the shell once, and then enter and slow the high density shell. In this case, the fuel reaches its maximum mass-weighted velocity at 22.53 ns, just before the stagnation shock enters the dense region. Prior to peak velocity, the inner portion of the shell and the fuel-ablator interface are stable to the Rayleigh-Taylor instability^{20,21}, but the ablation front is experiencing hydro-instability growth due to the ablative Rayleigh-Taylor instability²². The neutron production rate is shown at the bottom right of the figure. Here

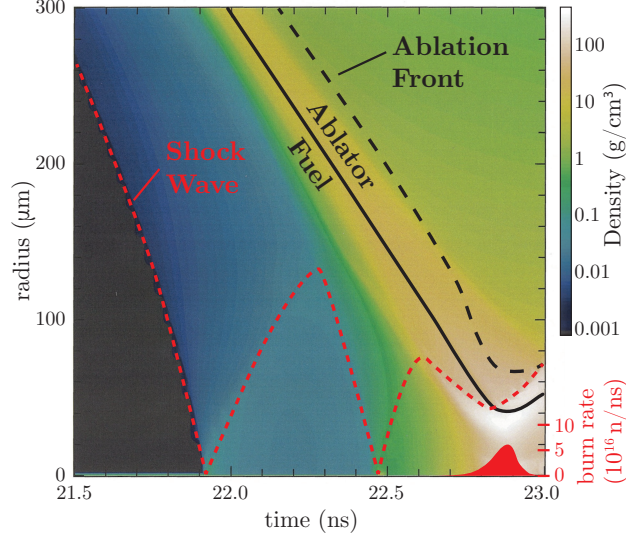


FIG. 1. (Color online) The deceleration stage in a 1D simulation of implosion N120321. The log of density is shown for the inner 300 μm and latest 1.5 ns of the implosion. The location of the shock wave, fuel-ablator interface, and ablation front (defined as the location of $e^{-1} \cdot \max(\text{density})$) are shown. Shown on the bottom right is the neutron production rate.

bang time occurs when the fuel-ablator interface reaches its minimum radius (*i.e.* when the fuel reaches its maximum compression).

The same late-stage is shown in Fig. 2 from the 3D simulation. A similar sequence of images is shown in Clark *et al.*¹¹, but is repeated here for clarity. These images show the ablation front surface colored by ion temperature. Cut-outs show the velocity magnitude and density. The hot spot is represented by the 1 keV isosurface, which is semi-transparent to show folds in the hot-spot structure. In Fig. 2(a), the shock wave has nearly reached the center of the capsule. Radiation asymmetries caused the shock wave to focus near the poles, creating local high temperature regions. In Fig. 2(b), a jet of material, mimicking the effect of the fill tube, is entering the interior of the capsule. This jet brings in both ablator material and colder DT and can be seen in Fig. 2(c) punching a hole through the hot spot. The stagnation shock begins traveling through the fuel in Fig. 2(c), increasing the density of the fuel. At this time, the capsule has become very prolate, with high density caps on each pole. This shape is characteristic of a Legendre-mode 2 radiation asymmetry. The most-prominent features on the ablation front are the perturbation seeded by the support tent and several spikes. By bang time, shown in Fig. 2(d), the shock has reached the ablation

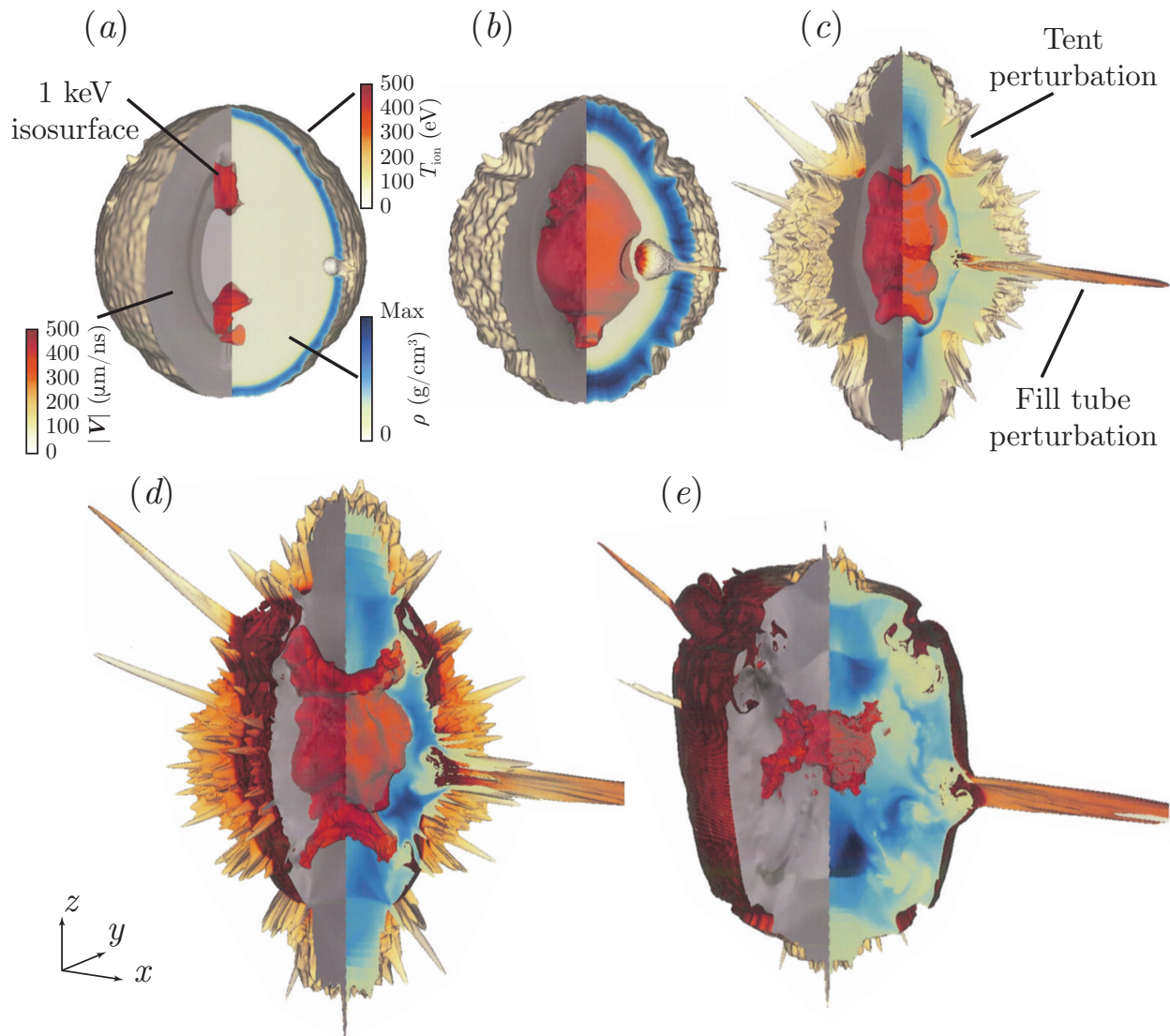


FIG. 2. (Color online) The deceleration stage in a 3D simulation of implosion N120321. The capsule is clipped to show the ablation front, colored by the ion temperature. A quarter of the capsule is removed to show the velocity magnitude on the left and the density on the right. The 1 keV isosurface, representing the boundary of the hot spot, is also shown. These images show the capsule at (a) 21.79 ns, (b) 22.36 ns, (c) 22.69 ns (0.17 ns after peak fuel velocity), (d), 22.81 ns (bang time), and (e) 22.90 ns. Spatial scales are different for each image.

front, as evident by the high temperature wave traveling through the spikes. The hot spot is in a distorted shape due to the radiation asymmetries and the support tent. Since the shock travels faster through the lower density regions in the shell caused by the radiation

asymmetries (shown next), the outward going shock gives the shell a cylindrical shape as the implosion evolves past bang time, as seen in Fig. 2(e). By this time the hot spot has radiated much of its energy and is shrinking in size.

III. STAGNATED FUEL SHAPE

The low-mode shape of the capsule is governed by asymmetries in the radiation field. The dominant effect in this case is a Legendre mode 2 asymmetry, which pushes harder on the waist of the capsule than on the pole, giving the capsule its prolate shape. The final shape at bang time is shown in Fig. 3(a) as a $4\text{-}\pi$ map of $\rho R(\theta, \phi) = \int \rho(r, \theta, \phi) dr$ from a 3D simulation including only radiation asymmetries. The $l = 2$ perturbation causes the ρR to vary from 3.6 g/cm² at the south pole, 1.8 g/cm² at the waist, and 3.4 g/cm² at the north pole. An $l = 4$ mode is also present, further reducing the ρR near 40° and 140°. Also present are perturbations around the azimuthal direction (m modes), with a contribution from the $m = 4$ mode that creates a ρR minimum of 1.0 g/cm² at $(\theta, \phi) = (40^\circ, 180^\circ)$. This minimum is the weak spot in the shell that allows the high pressure hot spot to vent, reducing the confinement time.

The ρR map from the 3D simulation that included asymmetries and other surface perturbations is shown in Fig. 3(b). This surface has finer structure due to surface perturbations, but overall looks very similar to the asymmetries-only case. The low ρR bands near $\theta = 40^\circ$ and 140° caused by the $l = 2$ and 4 radiation asymmetries lines up with the defect caused by the support tent. The fill tube causes a localized region of low ρR near $(\theta, \phi) = (80^\circ, 10^\circ)$. The full 3D simulation has an average ρR of 1.9 g/cm² (which matches the 1D simulation) and a standard deviation of 0.45 g/cm². The structure of the imploded fuel found in these simulations is in relative agreement with the experimental data from neutron activation diagnostics (NADs)²³. These diagnostics are sensitive to unscattered neutrons and therefore show the shape of the fuel assembly, as high ρR directions will have increased scatter. Low mode variations are observed from the NADs and show high concentration of fuel at the poles.

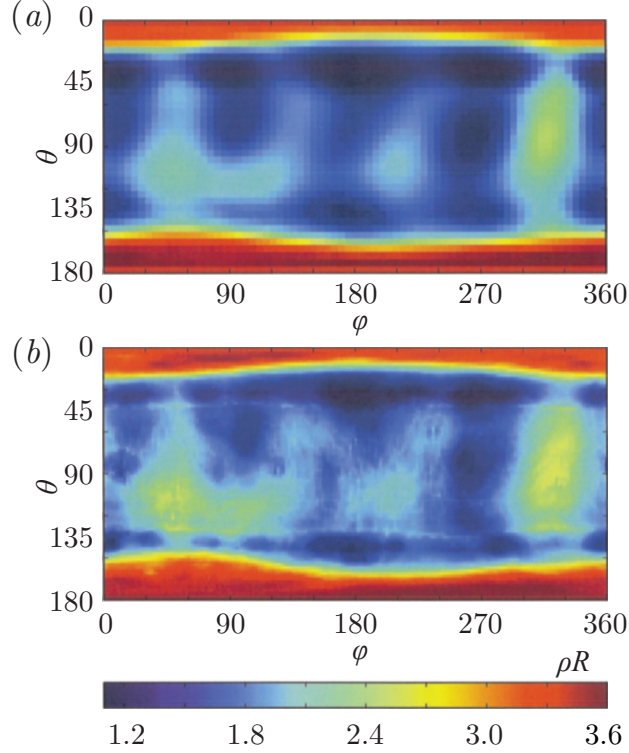


FIG. 3. (Color online) Map of ρR at bang time from (a) a 3D simulation including only radiation asymmetries and (b) from the 3D simulations which included asymmetries and other surface perturbations.

IV. FUEL AND HOT SPOT ENERGETICS

During deceleration, kinetic energy of the shell is converted into internal energy. This conversion is shown in Fig. 4(a), which shows the kinetic and internal energy in the DT fuel. This figure is comparing a 1D simulation with two 3D simulations. All three simulations contain 200 ng of ablator material pre-mixed into the capsule gas from the start of the simulation. One 3D simulation includes radiation asymmetries (“3D-asy”), while the other also includes all other perturbations (“3D”).

These simulations show the kinetic energy increasing up until the time of peak velocity, reaching 9.7 kJ at 22.53 ns. At this time the stagnation shock has formed at the inner surface of shell and begins slowing the fuel. The 3D simulation with all perturbations begins converting kinetic energy ~ 30 ps earlier than the 1D simulation as perturbations that have penetrated deeply are slowed earlier by the stagnation shock.

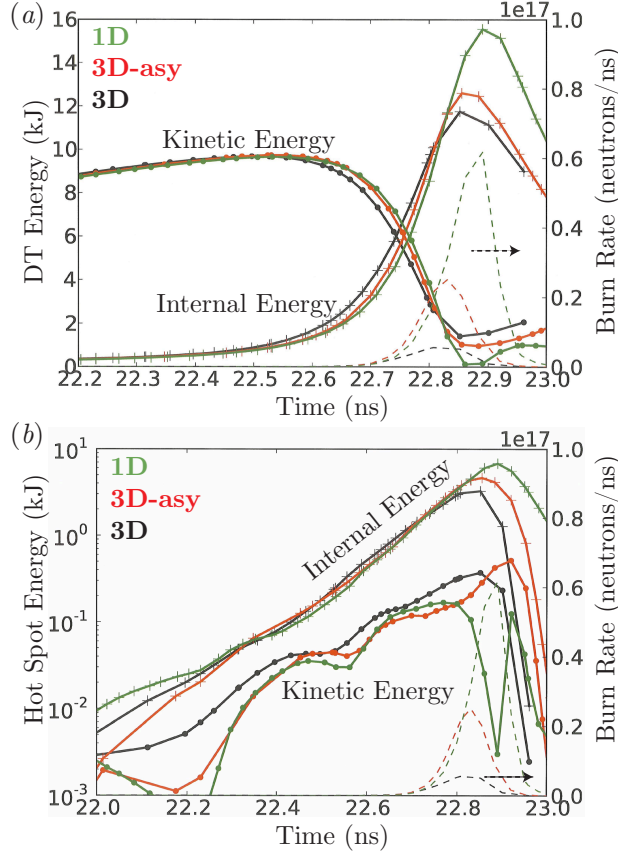


FIG. 4. (Color online) Kinetic and internal energy in (a) the DT fuel and (b) the hot spot (DT fuel > 1 keV). Three simulations are compared: a 1D simulation, a 3D simulation which included radiation asymmetries (“3D-asy”), and a 3D simulation that included radiation asymmetries and surface perturbations (“3D”). The dashed curves at the lower right of both figures report the DT fusion rate (right axis).

Asymmetries and perturbations cause kinetic energy to remain unconverted. The 1D simulation reaches a minimum of 0.12 kJ of kinetic energy, while 3D effects cause a minimum of 0.96 and 1.41 kJ of kinetic energy to remain for the 3D-asy and 3D cases, respectively. The average kinetic energy, weighted by the neutron production, is larger than these minimum values, with 3.31 kJ remaining in the 3D simulation. This kinetic energy lies in the high ρR directions of the shell, especially the polar caps, which do not fully stagnate and continue inwards.

Little of this remaining kinetic energy is contained in the hot spot. Figure 4(b) shows the kinetic and internal energy in the region greater than 1 keV. The 3D asymmetries-only

and full 3D simulations have burn-averaged hot-spot kinetic energies of 0.23 and 0.30 kJ, respectively. This compares with 3.72 and 2.65 kJ of internal energy in the hot spot for the two 3D cases.

While the kinetic energy in the hot spot is only 10% of the internal energy, there are still significant velocities present in the hot spot. Figure 5(a-c) shows the velocity magnitude at 22.56, 22.70, and 22.80 ns (bang time). Prior to stagnation, the hot spot is dominated by the near-isotropic swirling that is left behind by the shock wave that reflects from the center. When the fuel stagnates, large ρR perturbations are not fully stagnated and push flow through the hot spot. In this case, the largest ρR perturbations were the caps at the poles of the capsule. In Fig. 5(b), these polar caps are pushing two jets vertically towards each other. The upward-going jet has more momentum and dominates, resulting in upward and left pointing jet in Fig. 5(c). Figure 5(d) shows the burn-weighted velocity (*i.e.* averaging the velocity at a given time, weighted by the local neutron production rate, $n_D n_T \sigma \bar{\nu}$) and (e) the burn-weighted velocity standard deviation. As depicted in the images, the velocity is relatively isotropic early-on, as the average velocities are small ($<30 \mu\text{m}/\text{ns}$ from 22.5-22.7 ns) with a large standard deviation ($\sim 175 \mu\text{m}/\text{ns}$ in each direction). Closer to bang time, the flow is dominated by a bulk velocity with a burn-average of $91.2 \mu\text{m}/\text{ns}$ while the standard deviation has reduced to a burn-average of $192.0 \mu\text{m}/\text{ns}$ (quadrature sum over each direction). The bulk hot-spot velocity can be measured from a shift in the neutron spectra from neutron time-of-flight (NTOF) detectors. The magnitude of the bulk velocity observed in this experiment, $81 \pm 47 \mu\text{m}/\text{ns}$, agrees with the simulated value. The fidelity of the NTOF detectors has been upgraded recently to provided more accurate velocity measurements²⁴.

The standard deviation of the velocity can influence the measured temperature. Doppler effects broaden the width of the DT neutron spectrum through both velocity and thermal effects^{25,26}. The temperature that would have been measured from the width of the DT neutron spectrum (called T_{Brysk} ²⁷) for this simulation is 2.48 keV. This compares with the burn-averaged temperature (T_{ion}) of 2.02 keV. Since $\langle \sigma \bar{\nu} \rangle \propto T^{4.7}$ at these temperatures, using T_{Brysk} to estimate $\langle \sigma \bar{\nu} \rangle$ instead of T_{ion} would lead to an average reactivity $2.6\times$ larger than in actuality.

Using the larger value of T_{Brysk} in a static hot-spot model instead of T_{ion} leads to smaller

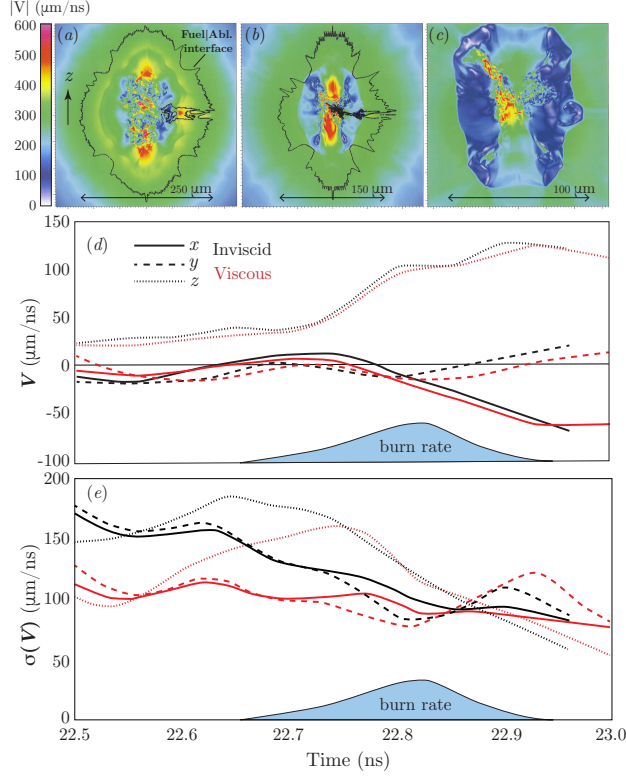


FIG. 5. (Color online) The velocity magnitude in the hot spot at (a) 22.56 ns, (b) 22.71 ns, and (c) 22.80 ns (bang time). In (a) and (b) a black line is showing the fuel-ablator interface. The burn-weighted velocity in the x , y , and z directions are shown in (d), while the standard deviation in each direction is shown in (e).

values of inferred hot-spot pressure. These models^{7,28} use the equation for the neutron yield,

$$Y_{DT} = \frac{n_{DT}^2 \langle \sigma \bar{v} \rangle V_{HS} t_{\text{burn}}}{4}, \quad (1)$$

to calculate the DT number density, n_{DT} , where t_{burn} is the burn width, and the hot spot volume, V_{HS} , is estimated from x-ray and neutron images. Since $P \propto n_{DT} T$ and $n_{DT} \propto \langle \sigma \bar{v} \rangle^{-1/2} \propto T^{-2.35}$, then $P \propto T^{-1.35}$. Therefore a static model of this implosion would calculate the hot spot pressure as being 31% lower than in actuality (the 3D simulation had a burn-averaged pressure of 250 Gbar). Similarly, the calculated energy needed to create this pressure through $p dV$ work, $E = (3/2) P V$, would be too low. This difference due to hot-spot velocity, along with the 3.3 kJ of residual kinetic energy in the high density fuel, may explain the “unaccounted energy” that static models of NIC implosions have reported¹.

Viscous effects play a role in dissipating some motion in the hot spot²⁹. The simulations

discussed previously were not including the effects of viscous dissipation, as common in ICF simulations. The late stage of the 3D simulation with asymmetries and perturbations was re-run with viscous dissipation effects included. The details of this comparison are discussed in Clark *et al.*¹¹, which show significant smoothing of the velocity field near the time of Fig. 5(a), but less prominent differences were observed near bang time. The burn-weighted velocities and standard deviations from the viscous simulation are also shown in Fig. 5(d,e) (red lines). Viscosity reduces the small scale motion that was left behind by the reflected shock wave, reducing the velocity standard deviation earlier in the stagnation phase. Near bang time, when the flow field is dominated by a few coherent jets, the viscous effects are less noticeable. By bang time, the kinetic energy in the hot spot has only reduced from 0.302 kJ to 0.298 kJ when viscous effects are included and the difference between T_{ion} and T_{Brysk} has only reduced from 460 eV to 440 eV.

V. JET INJECTION AND BREAKUP

As noted previously, this model contains a surface perturbation that injects a jet of ablator material into the hot spot. Jets of ablator material are thought to be common in ICF implosions, as x-ray images often exhibit bright spots that persist in time and travel through the hot spot, while spectral measurements show that these bright spots contain ablator material³⁰. The bright spot should initially travel from the location of a known surface defect, such as the fill tube, but this correlation is not always found³¹. Here we show the dynamics of this jet as it enters the hot spot. Figure 2 showed that this jet meets the hot spot shortly before the time of peak velocity and Fig. 5 showed the considerable motion present in the hot spot, therefore we can expect that this jet has a complex and 3D behavior.

Figure 6(a-d) shows an iso-surface between the DT and ablator material, colored by temperature. In Fig. 6(a), half of the shell is cut away to reveal the inward going jet. The tip of the jet has reached the hot spot at this time and its temperature is near 2 keV while the rest of this material interface is much cooler. Some of the material at the tip of the jet is being sheared away due to the velocity differential between the jet and the hot spot. In Fig. 6(b-d), the outer DT-ablator interface is also hidden to highlight the jet. At 22.74 ns (Fig. 6(b)), shearing effects have further broken apart the jet and small scale motion in this inviscid simulation has reduced the fragments to grid-scale sizes ($\sim 0.1 \mu\text{m}$). By bang

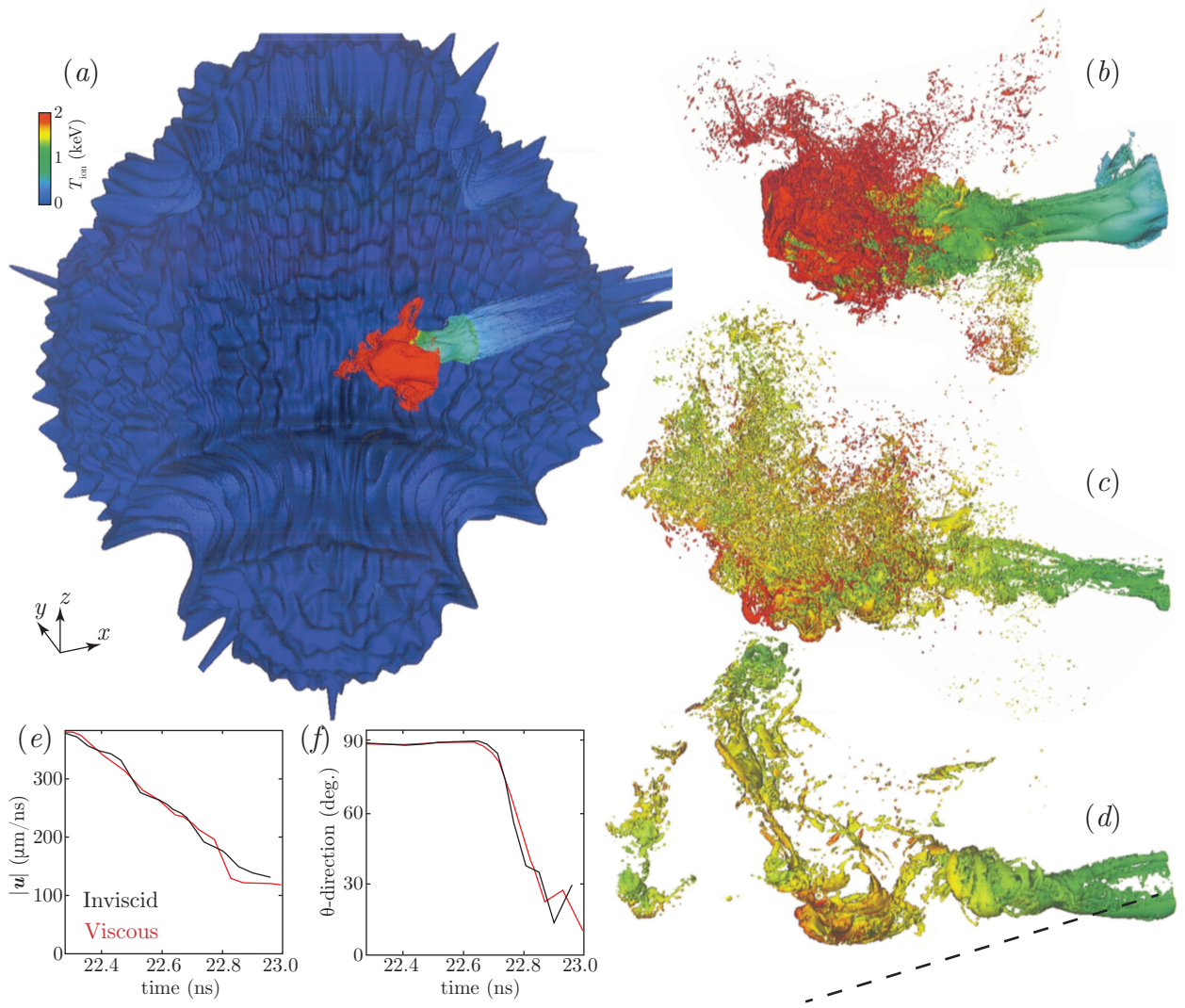


FIG. 6. (Color online) The jet of ablator material as it enters the hot spot. The jet is shown from the inviscid simulation at (a) 22.63 ns, (b) 22.74 ns, (c) 22.81 ns (bang time), and from the viscous simulation at (d) 22.81 ns. These show the fuel ablator interface with (a) half or (b-d) most of the interface hidden to reveal the jet. The interface is colored by temperature. Dashed line in (d) shows the original direction of the jet. The mass-weighted (e) speed and (f) θ -direction of the jet.

time, shown in Fig. 6(c), the jet has broken apart further, spreading the ablator material into a plume $\sim 60 \mu\text{m}$ wide. Figure 6(d) is also shown at bang time, but from the viscous simulation. Since the small scale motion of the hot spot has been reduced, the jet is less fragmented, yet it extends over a similar spatial extent as the inviscid simulation. The larger

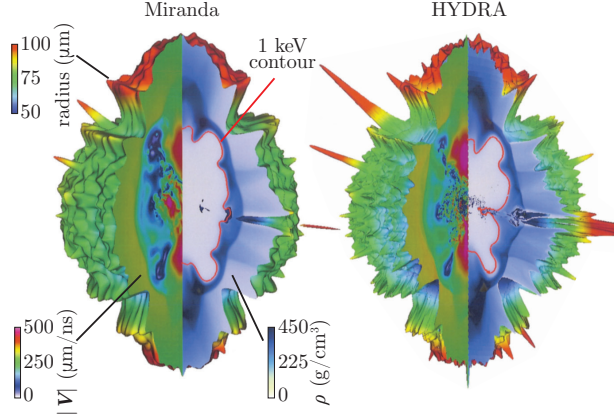


FIG. 7. (Color online) Comparison of inviscid Miranda and HYDRA simulations at 22.7 ns. The fuel-ablator interface is shown, colored by radius. The cut-outs show velocity magnitude on the left and density on the right. A contour showing the 1 keV hot spot boundary is also shown in the right cut-out.

ablator material fragments and smaller surface area in this viscous simulation cause it to heat up slower, but this is a small effect, changing the average temperature by only 8%. At these latter times, the trajectory of the jet has change due to the surrounding hot spot motion. The original direction of the jet is shown in Fig. 6(d) as a dashed line, yet the jet material has been pushed upwards in the $+z$ direction.

Figure 6(e,f) shows the mass-weighted average velocity and direction of the ablator material shown in Fig. 6(b-d). The jet is continually slowing down over this period, reaching 270 $\mu\text{m}/\text{ns}$ by bang time. Near 22.7 ns the jet starts changing direction. Originally the jet was traveling in the $\theta = 90^\circ$ direction (in the x - y plane), which is where the initial perturbation was located, but near 22.7 ns it begins traveling upwards. This change in direction is due to the bulk motion of the hot spot, which, as seen in Fig. 5(d), begins to flow in the $+z$ direction at this time. This change in direction would make it difficult to correlate a bright spot in the x-ray images caused by this jet to its original surface defect. These bright spots, however, may reveal the bulk motion of the hot spot.

VI. CODE COMPARISON

As a verification of the hydrodynamics observed during deceleration in this 3D model, the late stage of this implosion was also simulated using the Miranda code³². Miranda is a high-order Large Eddy Simulation (LES) code, specialized for mixing and hydro-instability simulations. The fundamentally different schemes between Miranda, with a fixed Eulerian grid and spectral-like accuracy, and HYDRA, employing Arbitrary Lagrange Euler (ALE) numerics, makes this an illuminating comparison. The flow field from the HYDRA simulation was linked into Miranda at 21.8 ns (shown in Fig. 2(a)). At this time, the ablation front is at a radius of 350 μm and the shock has nearly reached the center. Initializing at this time allows this simulation to capture the shock reflection and velocity field left behind in its wake. A similar comparison was made in Weber *et al.*²⁹ using an early, lower resolution version of the HYDRA 3D model for a different implosion. The simulation domain consists of a box with sides of 1300 μm and 512^3 uniformly spaced grid cells. The domain is refined periodically to follow the capsule as it converges. The simulation was run both without radiation transfer and with gray radiation diffusion and the non-radiative case was run with and without viscous effects.

Figure 7 shows a comparison of the Miranda and HYDRA simulations at 22.7 ns. Both codes show high velocities and similar structures in the hot spot. The stagnation shock is imparting a low-mode shape on the hot spot. The low mode shape of the fuel-ablator interface is very similar in Miranda, including the perturbation due to the tent and the high density polar caps. There are large-amplitude spikes on the interface in the HYDRA simulation whose amplitude is reduced in the Miranda simulation. The grid in Miranda simulation supports modes up to $l \sim 50$, which causes these spikes to be under-resolved. Yet we show below that the motion in the hot spot is well-resolved when viscous effects are included.

The transfer from kinetic to internal energy is shown in Fig. 8(a), comparing HYDRA to Miranda with the two radiation transfer options. Without the additional energy deposition during this period, the Miranda simulation without radiation transfer reaches 3% less peak kinetic energy. When gray radiation diffusion is used in Miranda, the DT fuel absorbs 8% more kinetic energy than in the more accurate multigroup diffusion HYDRA simulation. These two Miranda simulations bracket the HYDRA simulation and show that the transfer

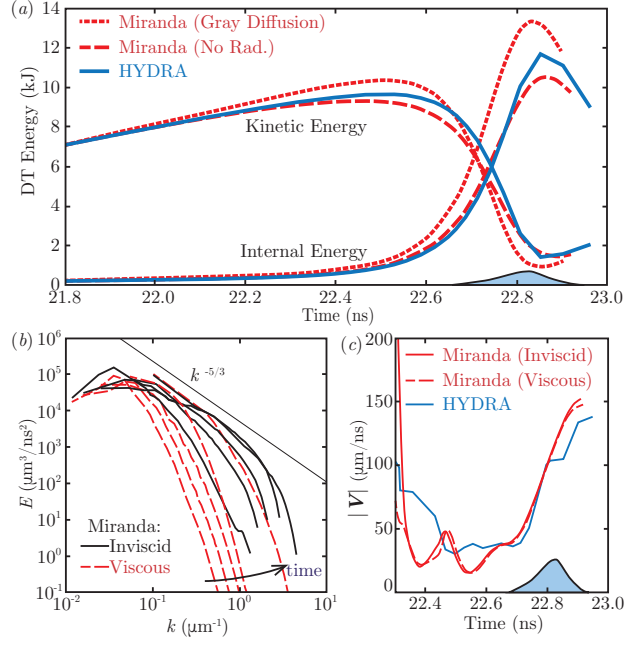


FIG. 8. (Color online) Comparison of the energetics in HYDRA and Miranda and Miranda simulations. (a) Kinetic and internal energy in the DT fuel from the HYDRA simulation and from Miranda simulations using gray radiation diffusion and without radiation transport. (b) Spectra of turbulent kinetic energy in the inviscid and viscous Miranda simulations (without radiation transport) from 22.2-22.8 ns. (c) Burn-weighted velocity magnitude from the HYDRA and inviscid and viscous Miranda simulations (without radiation transport). The DT reaction rate is shown on the lower right of (a) and (c).

to internal energy is very similar, with minima of 1-1.5 kJ of kinetic energy remaining unconverted, similar to the 1.4 kJ remaining in the HYDRA simulation. Grey diffusion also transports more energy from the hot spot to the dense fuel than in multigroup simulations and 1D simulations showed that neglecting radiation transport provided closer agreement to multigroup diffusion than gray diffusion during the last ~ 0.1 ns of the implosion. Therefore the Miranda case without radiation transport is used for the following comparisons.

The turbulent kinetic energy spectra is shown in Fig. 8(b) from the Miranda simulations with and without including viscous dissipation effects. The spectrum is computed by subtracting the 4π -averaged radial velocity, $V_r(r)$, to obtain the fluctuating velocity, $\mathbf{u}' = \mathbf{V} - V_r(r)$, and taking the power-spectral density from the box encompassing the hot spot. Without viscous effects, the spectrum is exhibiting a $k^{-5/3}$ slope at the later

times, indicating that it could be in a turbulent state. Viscous effects reduce the energy at the largest wavenumbers by orders of magnitude. This difference is more significant at the early times (22.2-22.6 ns) than at bang time (22.8 ns). The Reynolds number, $Re = |\mathbf{u}'| L/\nu$, is computed from an integral length scale, $L = \frac{3\pi}{2} \int k^{-1} E dk / \int E dk$, the rms velocity, $|\mathbf{u}'| = \sqrt{\frac{3}{2} \int E dk}$, and the average viscosity within the hot spot. The Reynolds number is $Re \approx 10$ near 22.2 ns and is increasing in time, reaching 300 by bang time.

The burn-weighted velocity magnitude is shown in Fig. 8(b) from the inviscid HYDRA simulation and the viscous and inviscid Miranda simulations. The Miranda simulations show little differences in the bulk velocity due to viscous effects. Both Miranda and HYDRA show the bulk velocity increasing ~ 0.1 ns prior to bang time, reaching ~ 100 $\mu\text{m}/\text{ns}$ at bang time.

VII. CONCLUSIONS

This work highlights the complex dynamics in ICF implosion that can only be captured in full-3D simulations. These simulations allow material to freely flow throughout the hot spot without the artificial symmetry boundary present in 2D or partial-3D simulations. This results in a striking amount of hot-spot motion, caused both by radiation asymmetries and from higher-mode features. These 3D effects influence the observable implosion signatures and therefore are essential to fully understand ICF implosions.

These simulations show that several kJ of energy remains as unstagnated kinetic energy. This residual energy is due to the large ρR variation of the fuel and not due to hot spot motion. The hot spot motion is well resolved, as viscous dissipation limits the range of length scales present in the hot spot. Despite the viscous nature of the hot spot, there is enough motion to broaden the DT neutron spectrum so that the observed average temperature rises from a thermal temperature of 2.02 keV to a Brysk temperature of 2.48 keV. There is also significant bulk motion in the hot spot near bang time as unstagnated features continue to travel inwards. This flow creates burn-averaged hot spot velocity near the ~ 100 $\mu\text{m}/\text{ns}$ values that are routinely measured in implosions.

The motion of a jet of ablator material into the hot spot is significantly affected by these 3D flows. Shearing effects and small-scale motion breaks apart the ablator material and spreads it throughout the hot spot, while bulk motion redirects the trajectory of the jet. These effects can influence the interpretation of bright spots seen in x-ray emissions and will

be necessary to quantify the amounts of atomic mixing that directly influence the output of CD symcap^{33,34} and similar experiments.

The favorable comparison of this model with results using the Miranda code suggests that these results are converged and not affected by the choice of numerics. Both codes show similar quantities of unconverted kinetic energy and hot spot motion. The turbulent kinetic energy spectrum in the Miranda simulation shows that, without viscosity, a turbulent flow field may be present, but viscous effects reduce the Reynolds number to 10-300 during deceleration.

ACKNOWLEDGEMENTS

This work was performed under the auspices of the U.S. Department of Energy by Lawrence Livermore National Laboratory under Contract No. DE-AC52-07NA27344.

REFERENCES

- ¹M. J. Edwards, P. K. Patel, J. D. Lindl, L. J. Atherton, S. H. Glenzer, S. W. Haan, J. D. Kilkenny, O. L. Landen, E. I. Moses, A. Nikroo, R. Petrasso, T. C. Sangster, P. T. Springer, S. Batha, R. Benedetti, L. Bernstein, R. Betti, D. L. Bleuel, T. R. Boehly, D. K. Bradley, J. A. Caggiano, D. A. Callahan, P. M. Celliers, C. J. Cerjan, K. C. Chen, D. S. Clark, G. W. Collins, E. L. Dewald, L. Divol, S. Dixit, T. Doeppner, D. H. Edgell, J. E. Fair, M. Farrell, R. J. Fortner, J. Frenje, M. G. Gatu Johnson, E. Giraldez, V. Y. Glebov, G. Grim, B. A. Hammel, A. V. Hamza, D. R. Harding, S. P. Hatchett, N. Hein, H. W. Herrmann, D. Hicks, D. E. Hinkel, M. Hoppe, W. W. Hsing, N. Izumi, B. Jacoby, O. S. Jones, D. Kalantar, R. Kauffman, J. L. Kline, J. P. Knauer, J. A. Koch, B. J. Koziolowski, G. Kyrala, K. N. LaFortune, S. L. Pape, R. J. Leeper, R. Lerche, T. Ma, B. J. MacGowan, A. J. MacKinnon, A. Macphée, E. R. Mapoles, M. M. Marinak, M. Mauldin, P. W. McKenty, M. Meezan, P. A. Michel, J. Milovich, J. D. Moody, M. Moran, D. H. Munro, C. L. Olson, K. Opachich, A. E. Pak, T. Parham, H.-S. Park, J. E. Ralph, S. P. Regan, B. Remington, H. Rinderknecht, H. F. Robey, M. Rosen, S. Ross, J. D. Salmonson, J. Sater, D. H. Schneider, F. H. Seguin, S. M. Sepke, D. A. Shaughnessy, V. A. Smalyuk, B. K. Spears, C. Stoeckl, W. Stoeffl, L. Suter, C. A. Thomas, R. Tommasini, R. P. Town,

- S. V. Weber, P. J. Wegner, K. Widman, M. Wilke, D. C. Wilson, C. B. Yeamans, and A. Zylstra, *Phys. Plasmas* **20**, 070501 (2013).
- ²V. A. Smalyuk, L. J. Atherton, L. R. Benedetti, R. Bionta, D. Bleuel, E. Bond, D. K. Bradley, J. Caggiano, D. A. Callahan, D. T. Casey, P. M. Celliers, C. J. Cerjan, D. Clark, E. L. Dewald, S. N. Dixit, T. Dppner, D. H. Edgell, M. J. Edwards, J. Frenje, M. Gatu-Johnson, V. Y. Glebov, S. Glenn, S. H. Glenzer, G. Grim, S. W. Haan, B. A. Hammel, E. P. Hartouni, R. Hatarik, S. Hatchett, D. G. Hicks, W. W. Hsing, N. Izumi, O. S. Jones, M. H. Key, S. F. Khan, J. D. Kilkenny, J. L. Kline, J. Knauer, G. A. Kyrala, O. L. Landen, S. Le Pape, J. D. Lindl, T. Ma, B. J. MacGowan, A. J. Mackinnon, A. G. MacPhee, J. McNaney, N. B. Meezan, J. D. Moody, A. Moore, M. Moran, E. I. Moses, A. Pak, T. Parham, H.-S. Park, P. K. Patel, R. Petrasso, J. E. Ralph, S. P. Regan, B. A. Remington, H. F. Robey, J. S. Ross, B. K. Spears, P. T. Springer, L. J. Suter, R. Tommasini, R. P. Town, S. V. Weber, and K. Widmann, *Phys. Rev. Lett.* **111**, 215001 (2013).
- ³J. Rygg, O. Jones, J. Field, M. Barrios, L. Benedetti, G. Collins, D. Eder, M. Edwards, J. Kline, J. Kroll, O. Landen, T. Ma, A. Pak, J. Peterson, K. Raman, R. Town, and D. Bradley, *Phys. Rev. Lett.* **112**, 195001 (2014).
- ⁴T. Ma, P. K. Patel, N. Izumi, P. T. Springer, M. H. Key, L. J. Atherton, L. R. Benedetti, D. K. Bradley, D. A. Callahan, and P. M. Celliers, *Phys. Rev. Lett.* **111**, 085004 (2013).
- ⁵S. P. Regan, R. Epstein, B. A. Hammel, L. J. Suter, H. A. Scott, M. A. Barrios, D. K. Bradley, D. A. Callahan, C. Cerjan, and G. W. Collins, *Phys. Rev. Lett.* **111**, 045001 (2013).
- ⁶S. W. Haan, J. D. Lindl, D. A. Callahan, D. S. Clark, J. D. Salmonson, B. A. Hammel, L. J. Atherton, R. C. Cook, M. J. Edwards, S. Glenzer, A. V. Hamza, S. P. Hatchett, M. C. Herrmann, D. E. Hinkel, D. D. Ho, H. Huang, O. S. Jones, J. Kline, G. Kyrala, O. L. Landen, B. J. MacGowan, M. M. Marinak, D. D. Meyerhofer, J. L. Milovich, K. A. Moreno, E. I. Moses, D. H. Munro, A. Nikroo, R. E. Olson, K. Peterson, S. M. Pollaine, J. E. Ralph, H. F. Robey, B. K. Spears, P. T. Springer, L. J. Suter, C. A. Thomas, R. P. Town, R. Vesey, S. V. Weber, H. L. Wilkens, and D. C. Wilson, *Phys. Plasmas* **18**, 051001 (2011).
- ⁷O. A. Hurricane, D. A. Callahan, D. T. Casey, P. M. Celliers, C. Cerjan, E. L. Dewald, T. R. Dittrich, T. Dppner, D. E. Hinkel, L. F. B. Hopkins, J. L. Kline, S. Le Pape, T. Ma,

- A. G. MacPhee, J. L. Milovich, A. Pak, H.-S. Park, P. K. Patel, B. A. Remington, J. D. Salmonson, P. T. Springer, and R. Tommasini, *Nature* **506**, 343 (2014).
- ⁸T. Dittrich, O. Hurricane, D. Callahan, E. Dewald, T. Dppner, D. Hinkel, L. Berzak Hopkins, S. Le Pape, T. Ma, J. Milovich, J. Moreno, P. Patel, H.-S. Park, B. Remington, J. Salmonson, and J. Kline, *Phys. Rev. Lett.* **112**, 055002 (2014).
- ⁹H.-S. Park, O. Hurricane, D. Callahan, D. Casey, E. Dewald, T. Dittrich, T. Dppner, D. Hinkel, L. Berzak Hopkins, S. Le Pape, T. Ma, P. Patel, B. Remington, H. Robey, J. Salmonson, and J. Kline, *Phys. Rev. Lett.* **112**, 055001 (2014).
- ¹⁰D. S. Clark, D. E. Hinkel, D. C. Eder, O. S. Jones, S. W. Haan, B. A. Hammel, M. M. Marinak, J. L. Milovich, H. F. Robey, L. J. Suter, and R. P. J. Town, *Phys. Plasmas* **20**, 056318 (2013).
- ¹¹D. S. Clark *et al.*, (2014), in preparation.
- ¹²A. L. Kritcher, R. Town, D. Bradley, D. Clark, B. Spears, O. Jones, S. Haan, P. T. Springer, J. Lindl, R. H. H. Scott, D. Callahan, M. J. Edwards, and O. L. Landen, *Phys. Plasmas* **21**, 042708 (2014).
- ¹³R. P. J. Town, D. K. Bradley, A. Kritcher, O. S. Jones, J. R. Rygg, R. Tommasini, M. Barrios, L. R. Benedetti, L. F. B. Hopkins, P. M. Celliers, T. Dppner, E. L. Dewald, D. C. Eder, J. E. Field, S. M. Glenn, N. Izumi, S. W. Haan, S. F. Khan, J. L. Kline, G. A. Kyrala, T. Ma, J. L. Milovich, J. D. Moody, S. R. Nagel, A. Pak, J. L. Peterson, H. F. Robey, J. S. Ross, R. H. H. Scott, B. K. Spears, M. J. Edwards, J. D. Kilkenny, and O. L. Landen, *Phys. Plasmas* **21**, 056313 (2014).
- ¹⁴S. R. Nagel *et al.*, (2014), in preparation.
- ¹⁵H. F. Robey, T. R. Boehly, P. M. Celliers, J. H. Eggert, D. Hicks, R. F. Smith, R. Collins, M. W. Bowers, K. G. Krauter, P. S. Datte, D. H. Munro, J. L. Milovich, O. S. Jones, P. A. Michel, C. A. Thomas, R. E. Olson, S. Pollaine, R. P. J. Town, S. Haan, D. Callahan, D. Clark, J. Edwards, J. L. Kline, S. Dixit, M. B. Schneider, E. L. Dewald, K. Widmann, J. D. Moody, T. Doppner, H. B. Radousky, A. Throop, D. Kalantar, P. DiNicola, A. Nikroo, J. J. Kroll, A. V. Hamza, J. B. Horner, S. D. Bhandarkar, E. Dzenitis, E. Alger, E. Giraldez, C. Castro, K. Moreno, C. Haynam, K. N. LaFortune, C. Widmayer, M. Shaw, K. Jancaitis, T. Parham, D. M. Holunga, C. F. Walters, B. Haid, E. R. Mapoles, J. Sater, C. R. Gibson, T. Malsbury, J. Fair, D. Trummer, K. R. Coffee, B. Burr, L. V. Berzins, C. Choate, S. J. Brereton, S. Azevedo, H. Chandrasekaran, D. C. Eder, N. D. Masters, A. C. Fisher, P. A.

- Sterne, B. K. Young, O. L. Landen, B. M. Van Wonterghem, B. J. MacGowan, J. Atherton, J. D. Lindl, D. D. Meyerhofer, and E. Moses, *Phys. Plasmas* **19**, 042706 (2012).
- ¹⁶D. G. Hicks, N. B. Meezan, E. L. Dewald, A. J. Mackinnon, R. E. Olson, D. A. Callahan, T. Dppner, L. R. Benedetti, D. K. Bradley, and P. M. Celliers, *Phys. Plasmas* **19**, 122702 (2012).
- ¹⁷S. H. Glenzer *et al.*, *Phys. Plasmas* **19**, 056318 (2012).
- ¹⁸O. S. Jones, C. J. Cerjan, M. M. Marinak, J. L. Milovich, H. F. Robey, P. T. Springer, L. R. Benedetti, D. L. Bleuel, E. J. Bond, D. K. Bradley, D. A. Callahan, J. A. Caggiano, P. M. Celliers, D. S. Clark, S. M. Dixit, T. Doppner, R. J. Dylla-Spears, E. G. Dzentitis, D. R. Farley, S. M. Glenn, S. H. Glenzer, S. W. Haan, B. J. Haid, C. A. Haynam, D. G. Hicks, B. J. Kozioziemski, K. N. LaFortune, O. L. Landen, E. R. Mapoles, A. J. MacKinnon, J. M. McNaney, N. B. Meezan, P. A. Michel, J. D. Moody, M. J. Moran, D. H. Munro, M. V. Patel, T. G. Parham, J. D. Sater, S. M. Sepke, B. K. Spears, R. P. J. Town, S. V. Weber, K. Widmann, C. C. Widmayer, E. A. Williams, L. J. Atherton, M. J. Edwards, J. D. Lindl, B. J. MacGowan, L. J. Suter, R. E. Olson, H. W. Herrmann, J. L. Kline, G. A. Kyrala, D. C. Wilson, J. Frenje, T. R. Boehly, V. Glebov, J. P. Knauer, A. Nikroo, H. Wilkens, and J. D. Kilkenny, *Phys. Plasmas* **19**, 056315 (2012).
- ¹⁹M. M. Marinak, G. D. Kerbel, N. A. Gentile, O. Jones, D. Munro, S. Pollaine, T. R. Dittrich, and S. W. Haan, *Phys. Plasmas* **8**, 2275 (2001).
- ²⁰L. Rayleigh, *Proc. R. Soc. London, Ser. A* **14**, 170 (1883).
- ²¹G. I. Taylor, *Proc. R. Soc. London, Ser. A* **201**, 192 (1950).
- ²²R. Betti, V. N. Goncharov, R. L. McCrory, P. Sorokin, and C. P. Verdon, *Phys. Plasmas* **3**, 2122 (1996).
- ²³D. L. Bleuel, C. B. Yeamans, L. A. Bernstein, R. M. Bionta, J. A. Caggiano, D. T. Casey, G. W. Cooper, O. B. Drury, J. A. Frenje, C. A. Hagmann, R. Hatarik, J. P. Knauer, M. G. Johnson, K. M. Knittel, R. J. Leeper, J. M. McNaney, M. Moran, C. L. Ruiz, and D. H. G. Schneider, *Rev. Sci. Instrum.* **83**, 10D313 (2012).
- ²⁴B. K. Spears, M. J. Edwards, S. Hatchett, J. Kilkenny, J. Knauer, A. Kritcher, J. Lindl, D. Munro, P. Patel, H. F. Robey, and R. P. J. Town, *Phys. Plasmas* **21**, 042702 (2014).
- ²⁵B. Appelbe and J. Chittenden, *Plasma Physics and Controlled Fusion* **53**, 045002 (2011).
- ²⁶T. J. Murphy, *Phys. Plasmas* **21**, 072701 (2014).
- ²⁷H. Brysk, *Plasma Physics* **15**, 611 (1973).

- ²⁸C. Cerjan, P. T. Springer, and S. M. Sepke, Phys. Plasmas **20**, 056319 (2013).
- ²⁹C. R. Weber, D. S. Clark, A. W. Cook, L. E. Busby, and H. F. Robey, Phys. Rev. E **89**, 053106 (2014).
- ³⁰G. A. Kyrala, S. Dixit, S. Glenzer, D. Kalantar, D. Bradley, N. Izumi, N. Meezan, O. L. Landen, D. Callahan, and S. V. Weber, Rev. Sci. Instrum. **81**, 10E316 (2010).
- ³¹M. A. Barrios, S. P. Regan, L. J. Suter, S. Glenn, L. R. Benedetti, D. K. Bradley, G. W. Collins, R. Epstein, B. A. Hammel, G. A. Kyrala, N. Izumi, T. Ma, H. Scott, and V. A. Smalyuk, Phys. Plasmas **20**, 072706 (2013).
- ³²A. W. Cook, Phys. Fluids **19**, 055103 (2007).
- ³³V. Smalyuk, R. Tipton, J. Pino, D. Casey, G. Grim, B. Remington, D. Rowley, S. Weber, M. Barrios, L. Benedetti, D. Bleuel, D. Bradley, J. Caggiano, D. Callahan, C. Cerjan, D. Clark, D. Edgell, M. Edwards, J. Frenje, M. Gatu-Johnson, V. Glebov, S. Glenn, S. Haan, A. Hamza, R. Hatarik, W. Hsing, N. Izumi, S. Khan, J. Kilkenny, J. Kline, J. Knauer, O. Landen, T. Ma, J. McNaney, M. Mintz, A. Moore, A. Nikroo, A. Pak, T. Parham, R. Petrasso, D. Sayre, M. Schneider, R. Tommasini, R. Town, K. Widmann, D. Wilson, and C. Yeamans, Physical Review Letters **112**, 025002 (2014).
- ³⁴D. T. Casey, V. A. Smalyuk, R. E. Tipton, J. E. Pino, G. P. Grim, B. A. Remington, D. P. Rowley, S. V. Weber, M. Barrios, L. R. Benedetti, D. L. Bleuel, E. J. Bond, D. K. Bradley, J. A. Caggiano, D. A. Callahan, C. J. Cerjan, K. C. Chen, D. H. Edgell, M. J. Edwards, D. Fittinghoff, J. A. Frenje, M. Gatu-Johnson, V. Y. Glebov, S. Glenn, N. Guler, S. W. Haan, A. Hamza, R. Hatarik, H. W. Herrmann, D. Hoover, W. W. Hsing, N. Izumi, P. Kervin, S. Khan, J. D. Kilkenny, J. Kline, J. Knauer, G. Kyrala, O. L. Landen, T. Ma, A. G. MacPhee, J. M. McNaney, M. Mintz, A. Moore, A. Nikroo, A. Pak, T. Parham, R. Petrasso, H. G. Rinderknecht, D. B. Sayre, M. Schneider, W. Stoeffl, R. Tommasini, R. P. Town, K. Widmann, D. C. Wilson, and C. B. Yeamans, Physics of Plasmas (1994-present) **21**, 092705 (2014).